ACS APPLIED ENERGY MATERIALS

www.acsaem.org Article

Excellent Metal Phosphide Electrode for Potassium Ion Hybrid Capacitors: The Case of Carbon Nanotube-Wrapped AgP_2

Jia-Zheng Yen, Che-Bin Chang, Kai-Siang Jhang, and Hsing-Yu Tuan*

Cite This: *ACS Appl. Energy Mater.* 2023, 6, 822−831 Read Online

ACCESS | Metrics & More | Article Recommendations | Supporting Information

ABSTRACT: Potassium-ion hybrid capacitors (PIHCs) have received extensive attention due to combining the advantages of high energy density of batteries and high power density of capacitors and are economically advantageous alternatives to lithium-ion hybrid capacitors. Metal phosphides are potential anode materials for K^+-storage with high theoretical capacity, relatively low working potential, thermal stability, and metal characteristics. Nevertheless, high-performance metal phosphide materials for PIHC applications have proven to be challenging due in part to the dissatisfied electronic conductivity, irreversible deterioration of the structure, and high electron transfer resistance. In this work, we synthesize carbon nanotube (CNT)-wrapped AgP_2 via a wet-ball milling (WBM) approach to prepare the electrode slurry. Simultaneously with electrode cycling, the in situ formed Ag nanocrystals increased the electrical conductivity and formed Ag-P composites that easily adsorbed more K^+, the framework of CNTs effectively reduced the capacity fading caused by material refinement, and a large surface area is provided to facilitate electrolyte penetration. Owing to these advantageous merits of AgP_2/CNT electrodes, the assembled PIHC exhibits a high energy/power density of 37.3 Wh kg^{-1}/12207.3 W kg^{-1}, respectively, and remarkable cycling life over 2000 cycles. These promising results reveal that the design interfacial engineering of the CNT-wrapped AgP_2 scaffold provides a clue to propel the development of metal phosphide-based hybrid capacitors.

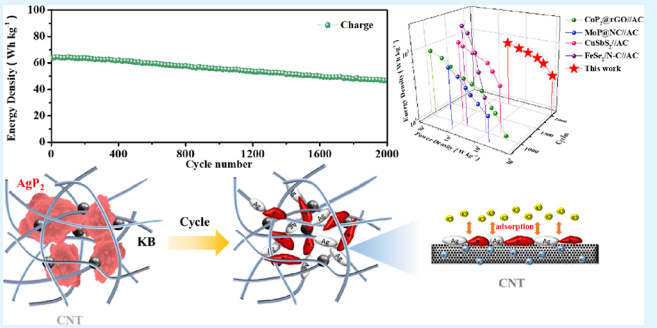

KEYWORDS: *metal phosphide, multi-walled carbon nanotubes, potassium ion, hybrid capacitors, energy storage*

1. INTRODUCTION

Lithium-ion batteries (LIBs), with energy density (>120 Wh kg^{-1}) and voltage (>3.6 V), outstanding rate capability, and low self-discharge, are currently the state-of-the-art technology for high-energy electrochemical storage, which increased the demand for lithium (from 31,700 tons in 2014 to 77,000 tons in 2019).[1] However, the rarity and uneven global distribution of lithium limit the development of LIBs.[2] The potassium-ion energy storage prototype is considered as a potential replacement for the lithium-ion energy storage system proposed by Ali Eftekhari in 2004. Potassium has the following advantages: (i) abundant chemical elements (2.09 wt % in the earth's crust); (ii) even global distribution; (iii) high standard reduction potential of K^+/K (−2.93 V vs SHE); and (iv) cheap current collector ($2042/t in Al foil, $7951/t in Cu foil).[3−6] Unfortunately, the stability of the potassium-ion energy storage system remains inferior to the lithium system.[7] To close the performance gap, the development of potassium-ion energy storage electrode materials with excellent cycling and rate performance is still challenging.[6]

Due to the promise of extremely high theoretical capacity (2594 mA h g^{-1} in K_3P), phosphorous is regarded as possible anode in K^+-storage devices.[8] However, the key challenges associated with phosphorus are inherently low electronic conductivity (~10^{-14} S cm^{-1}) and pronounced volume change during charge/discharge (~595%), leading to capacity fading and poor rate performance.[9,10] Metal phosphide materials have lower volume change and higher electronic conductivity than phosphorus.[11−13] In addition, the nanosize metal phosphides have a shorter ionic transfer pathway, more active sites to facilitate kinetic properties, and fast ionic conductivity in PIHCs.[14−17] For example, Wang et al. assembled Co_2P@rGO//AC to show an energy density of 87 Wh kg^{-1} at a power density of 12 W kg^{-1} with a lifespan of over 1000 cycles.[18] Nonetheless, pronounced volume changes during charge/discharge not only lead to severe pulverization of the electrode but also are challenging to form a stable protective layer to keep the solid electrolyte interface (SEI).[19,20] Furthermore, the electronic conductivity of metal phosphides (Co_2P) is still

Received: September 23, 2022
Accepted: December 20, 2022
Published: January 3, 2023

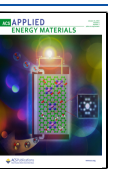

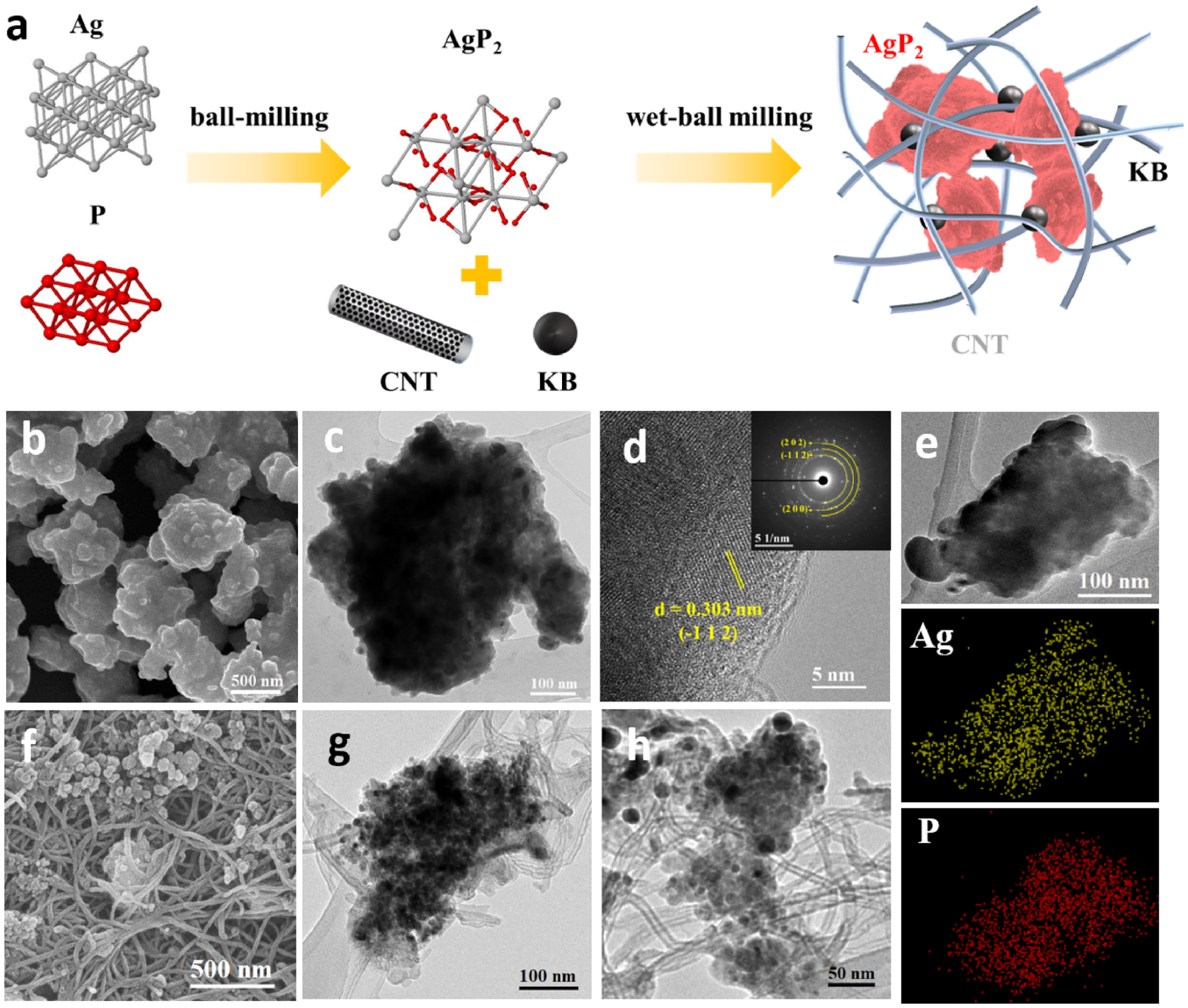

Figure 1. (a) Illustration of the preparation of AgP_2/CNT. Morphology characterization in (b) SEM image, (c, d) TEM images, and (e) EDS elemental mapping of AgP_2. (f) SEM and (g, h) TEM images of AgP_2/CNT.

unsatisfactory for PIHCs with moderate rate capability. Therefore, reports on metal phosphide material PIHCs are very limited.[11]

To achieve high-performance PIHCs, it is crucial to balance the dynamical properties between the adsorption/desorption process that occurred in the cathode and the sluggish faradaic reaction that occurred in the anode.[21] The rapid K^+ insertion/extraction property is important because anode materials directly determine the rate capability and cycling stability of the PIHC.[22−25] To overcome these problems, recent energy storage studies have shown that constructing active material/carbon heterostructures is considered one of the most promising strategies.[26−30] Several types of carbon-based materials as a buffer for volume change of electrodes have been developed, such as graphite, graphene, doped carbon, hard carbon/soft carbon, and CNTs.[31−33] Among those carbon-based materials, graphene has excellent electrical conductivity and flexible two-dimensional structure due to simple molecular sheets of sp^2 carbon atoms. Moreover, a sheet of graphene is rolled into a tube or cylinder shape and the weak van der Waals interactions occur between graphene layers to form various CNTs including single-walled CNTs, double-walled CNTs, and multi-walled CNTs. CNTs have distinct properties of mechanical strength, aspect ratio, and thermal and electrical conductivities, which are an effective mechanical support and simultaneously provide a 1D electron conducting pathway.[34,35] The interfacial engineering of carbon nanotubes with active materials effectively buffers volume changes, prevents active material agglomeration, and provides electron/ion transport channels during long-term cycling, which play a crucial role in improving energy storage performance and ensuring the structural stability of electrodes.[36−40] For example, MoP/C and TiO_2@CNT@C show high energy/power density in sodium-ion capacitors.[41,42] Obviously, this design achieves good compatibility for high electrochemical performance in capacitor devices. However, the structure of CNTs may be destroyed by drastic processes such as dry ball milling, which limits the extensiveness of the synthesis process.

In this study, we propose wet-ball milling (WBM) to prepare electrode slurries, including AgP_2 and CNTs as phosphide-

https://doi.org/10.1021/acsaem.2c03113
ACS Appl. Energy Mater. 2023, 6, 822−831

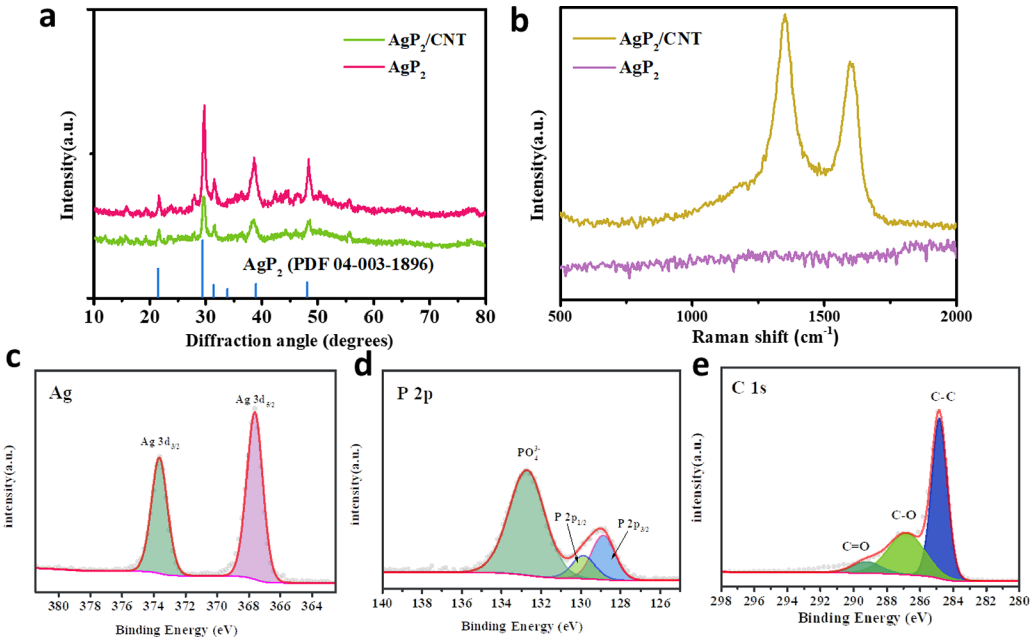

Figure 2. Material characterization of (a) XRD patterns and (b) Raman spectra of CNT, AgP_2, and AgP_2/CNT composites. (c–e) High-resolution XPS spectrum of (c) Ag, (d) P, and (e) C of AgP_2/CNT.

based electrodes for improving the electronic conductivity and structural stability of PHICs. During K^+ electrochemical activation, the Ag nanocrystals were formed in situ that not only increase the conductivity but also promote the refinement of the material and increase active sites. Notably, the interfacial engineering of CNT-encapsulated AgP_2 enhanced electrical conductivity, facilitated electrolyte penetration, and provided a large surface area and active sites for K^+ adsorption/desorption and enhanced electron/ion transport. Benefitting from these merits, the as-prepared AgP_2/CNT electrode shows a reversible capacity of 440 mA h g^{-1} at a current density of 100 mA g^{-1} and a capacity of 150 mA h g^{-1} is obtained at a high current density of 3 A g^{-1} in the potassium ion battery. The PIHC consisting of the commercial-activated carbon (AC) cathode and AgP_2/CNT anode exhibits an excellent energy density of 46.3 Wh kg^{-1} after 2000 cycles at a current density of 1 A g^{-1} and a high energy/power density of 37.3 Wh kg^{-1}/12207.3 W kg^{-1}, respectively. Consequently, the results of the PIHC demonstrate that the metal phosphide-based PIHC presented an exceptionally high energy and power density as well as long cycling stability with interfacial engineering of in situ formed Ag-P composites with the CNT framework.

2. EXPERIMENTAL SECTION

2.1. Materials. Red phosphorus (P), silver (Ag), sodium carboxymethyl cellulose (NaCMC, average M_w = 700,000), dimethyl ether (DME, ≥99.8%), and potassium metal (in mineral oil, 98%) were purchased from Sigma-Aldrich. Potassium bis(fluorosulfonyl)-imide (KFSI, 97%) was purchased from Combi-Blocks. Active carbon was purchased from Kuraray Chemical Company. Carbon nanotubes were purchased from Golden Innovation Business Co., Ltd. Ketjen Black EC600jd (KB) was purchased from Lion Specialty Chemicals. Copper and aluminum foil were purchased from Chang-Chun group. Coin-type cell CR2032 was purchased from Shining Energy. Glass fiber (diameter = 19 mm) was purchased from Advantec.

2.2. Synthesis of AgP_2. The AgP_2 powder was synthesized via the high-energy ball milling process under an Ar atmosphere. Ag powder (216 mg) and 124 mg of P powder were added in a stainless-steel milling jar (12 mL) along with stainless steel balls; the weight ratio of the stainless steel ball to Ag and P powder was about 30:1. The mixture was ball-milled by a planetary ball mill (RETSCH PM100) for 24 h with a rotational speed at 400 rpm.

2.3. Material Characterization. The X-ray diffractometer (XRD, Bruker, D8) data were obtained with Cu-Kα radiation. All materials were characterized by using scanning electron microscopy (SEM, HITACHI-SU8010). Transmission electron microscopy (TEM, JEOL, JEM-ARM200FTH) services were provided by NTHU, and JOEL (JEM-F200) services were provided by NCTH. To obtain high-resolution TEM (HRTEM) images of materials, an accelerating voltage of 200 kV for investigating further structure analysis including morphology, energy-dispersive spectroscopy (EDS), SAED, and HRTEM was used. The XPS characteristic peaks were conducted with ULVAC-PHI Quantera II. All the spectra obtained from XPS analysis were first calibrated by referencing the binding energy of C 1s (284.8 eV) followed by curve fitting using the software XPSPEAK VER. 4.1.

2.4. Electrochemical Characterization. The electrode slurry was prepared by mixing active materials, CNTs, KB, and NaCMC binder in a ratio of 50:15:10:25 into a stainless steel. Then, distilled water was injected into the stainless steel to form a homogeneous slurry at 200 rpm for 12 h. The loading of AgP_2 on the copper foil was approximately 0.6–1.0 mg cm^{-2}. For the fabrication of the cathode electrode for PHIC, polyvinyldifluoride (PVDF), super P, and active carbon were added in *N*-methyl-2-pyrrolidone (NMP) at a ratio of 8:1:1. The loading of active carbon on the aluminum foil was approximately 0.8–1.2 mg cm^{-2}. The half-cell (CR2032) was made in a glovebox filled with Ar gas. The electrolyte was 1 M KFSI in DMC added to infiltrate the anode electrode, a glass fiber separator was added, and K metal foil was used as a counter electrode. The galvanostatic charge/discharge tests were conducted in the voltage range of 0.01–3.0 V in a battery measurement system (NEWARE CT-4000). Cyclic voltammetry (CV) tests and electrochemical impedance spectroscopy (EIS) tests were obtained on a Biologic-Science Instruments VMP3 workstation.

3. RESULTS AND DISCUSSION

The AgP_2/CNT composites were prepared by a ball milling process, as illustrated in Figure 1a. The morphologies of AgP_2 and AgP_2/CNT were observed by scanning electron

https://doi.org/10.1021/acsaem.2c03113
ACS Appl. Energy Mater. 2023, 6, 822–831

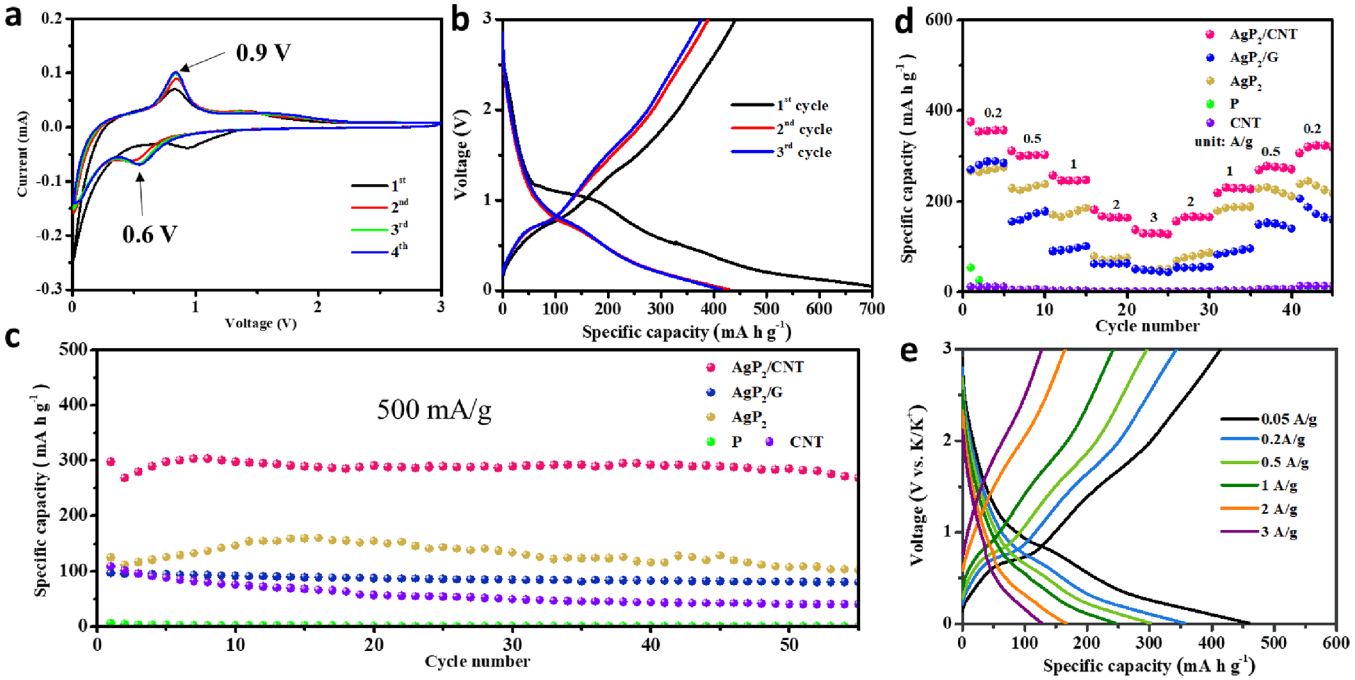

Figure 3. Electrochemical performances of AgP_2/CNT in the potassium ion half-cell. (a) CV curves of AgP_2/CNT at 0.1 mV s^{-1}. (b) Galvanostatic charge/discharge curves of AgP_2/CNT at a current density of 100 mA g^{-1}; (c) Cycling performance of AgP_2/CNT, AgP_2/G, AgP_2, P, and CNT at a current density of 500 mA g^{-1}. (d) Rate capability of AgP_2, AgP_2/G, AgP_2/CNT, CNT, and P at various rates. (e) Galvanostatic charge/discharge profiles of AgP_2/CNT at different current densities.

microscopy (SEM), as shown in Figure 1b,f. The particle size for AgP_2 was observed to be approximately 400−700 nm after ball milling and slight aggregation (Figure 1b). As shown in Figure 1f, the AgP_2 uniformly dispersed into the conductive framework constructed by CNTs in the AgP_2/CNT composites. As expected, the results indicate that CNTs blended with NaCMC and still kept the original morphologies (Figure S1a), which provide continuous electrical pathways and a tough framework. The microstructure of AgP_2 was investigated by the selected area electron diffraction (SAED) pattern and transmission electron microscopy (TEM) image. Figure 1c shows the HRTEM image of AgP_2 showing its irregular particle. Crystalline lattice fringes with a spacing of 0.303 nm were revealed by TEM at the interface of AgP_2 particles in Figure 1d. Further evidence for AgP_2 is obtained by the SAED pattern, indicating the microstructural characteristics of AgP_2 (PDF 04-003-1896), where the (−112), (200), and (202) diffraction planes with *d*-spacing are 0.303, 0.285, and 0.189 nm, respectively. The elemental distribution determined by the HRTEM-EDS spectrum and elemental mapping is shown in Figure 1e. The elements of Ag and P are equivalently mixed in the as-prepared AgP_2. Figure 1g,h shows the TEM image of the AgP_2/CNT composite, confirming the success of interfacial engineering where the particle size of the AgP_2/CNT composite is smaller than the pristine AgP_2.

The XRD patterns of the AgP_2 and AgP_2/CNT composite are shown in Figure 2a. The diffraction peaks at 29.4, 38.9, and 48.0° can be indexed to (−112), (200), and (202) planes of AgP_2 (PDF 04-003-1896), respectively. The similar XRD patterns of the AgP_2 and AgP_2/CNT composite indicate no side reactions after WBM. Moreover, the weak intensity of the AgP_2/CNT peaks in XRD patterns is ascribed to CNTs shading the signal of X-ray. Raman spectra were collected on the AgP_2 and AgP_2/CNT composite (Figure 2b). The Raman spectrum shows intense bands of the G and D bands of AgP_2/CNT at 1591.6 and 1332.8 cm^{-1}, respectively, indicating the characteristic signal of CNTs (Figure S1d). In contrast, AgP_2 has no obvious signals of the D and G bands, validating the existence of CNTs on the material. The X-ray photoelectron spectroscopy (XPS) analysis was performed to study the surface chemistry of AgP_2/CNT. Figure 2c−e demonstrates the high revolution Ag 3d, P, and C XPS peaks of the AgP_2/CNT composite, respectively. The Ag 3d spectrum is shown in Figure 2c, and the peaks at 367.6 eV (Ag $3d_{5/2}$) and 373.6 eV (Ag $3d_{3/2}$) can be indexed to Ag^+. In the P 2p XPS spectrum (Figure 2d), the peak at 129.0 eV can be separated into P $2p_{3/2}$ and P $2p_{1/2}$ peaks at 128.9 and 129.9 eV, respectively. Moreover, the peak located at ∼132.7 eV can be attributed to PO_4^{3-} species, indicating the slight oxidation on the surface of AgP_2 in air, which should be stored in inert gas to prevent deterioration.[43] In the C XPS spectrum (Figure 2e), the peak can be deconvoluted into three peaks centered at 284.8, 286.8, and 289.2 eV that are assigned to C−C, C−O, and C═O bonds, respectively, which are derived from noise interference or CNTs.

The electrochemical performances of the half-cell of the AgP_2/CNT electrodes are summarized in Figure 3. Figure 3a demonstrates the cyclic voltammetry (CV) performance of the AgP_2/CNT electrode for the first four cycles between 0.01 and 3.0 V at a scan rate of 0.1 mV s^{-1}. An irreversible peak appears at ∼1.0 V during the first cycle that can be interpreted as the formation of a SEI and the in situ formed Ag nanocrystals. After the second cycling, the discharge profiles show a peak at ∼0.6 V and charge profiles show a peak at ∼0.9 V, indicating the reversible potassiation and the depotassiation process. In the following scans, the CV curves are highly reversible and overlapped, indicating the high electrochemical reversibility of the AgP_2/CNT. The charge/discharge voltage profiles of

https://doi.org/10.1021/acsaem.2c03113
ACS Appl. Energy Mater. 2023, 6, 822−831

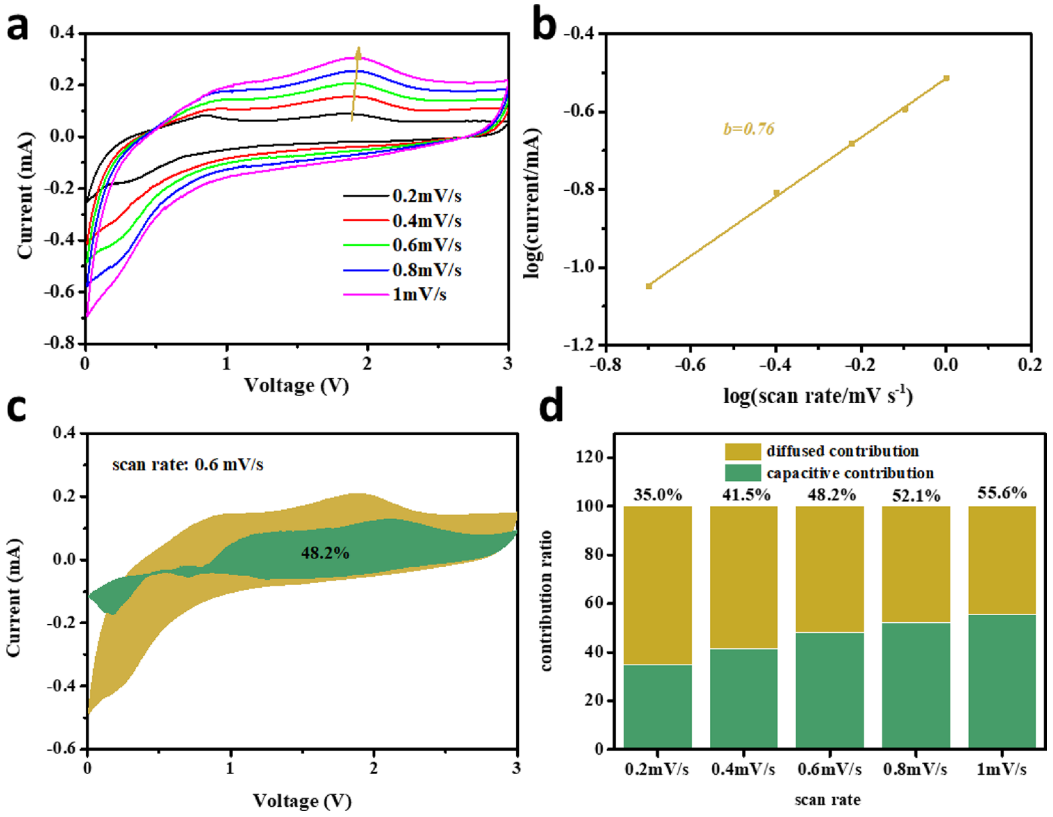

Figure 4. Kinetic analyses of the K^+-storage behaviors for the AgP_2/CNT electrode. (a) CV cures at stepwise different scan rates from 0.2 to 1.0 mV s^{-1}. (b) Corresponding b values in linear regression. (c) Capacitive contribution (green section) at 0.6 mV s^{-1} AgP_2/CNT. (d) Ratio of diffused contribution and capacitive contribution at five different scan rates of AgP_2/CNT.

AgP_2/CNT at 100 mA g^{-1} are shown in Figure 3b. Consistent with the CV data, the plateau is mainly around 0.7−0.9 V during charging, and the plateau is mainly around 1.0−0.5 V during discharging. The cycling performance of AgP_2/CNT at 100 mA g^{-1} is shown in Figure S4a, exhibiting a capacity of 383.2 mAh g^{-1}, indicating the high reversible capacity of AgP_2/CNT. We test the cycling performance of AgP_2, AgP_2/G, AgP_2/CNT, CNT, and P at 500 mA g^{-1} (Figure 3c). As expected, the AgP_2/CNT electrode exhibits excellent stable cycling performance and the capacity remained at 280.5 mAh g^{-1} after 55 cycles. For comparison, the AgP_2 electrode exhibits a capacity at 107.6 mAh g^{-1} without interfacial engineering of CNTs. On the other hand, the AgP_2/G electrode exhibits a capacity at 79.4 mAh g^{-1}, which indicates that the layer of graphite cannot improve the performance of AgP_2. The rate performance of AgP_2, AgP_2/G, AgP_2/CNT, CNT, and P electrodes at different current densities clearly demonstrates the superior behavior of interfacial engineering in Figure 3d. For the AgP_2/CNT electrode, reversible capacities of 352.9, 301.7, 245.6, 166.6, and 128.4 mAh g^{-1} can be obtained at current densities of 0.2, 0.5, 1, 2, and 3 A g^{-1}, respectively, which are demonstrated in the charge and discharge curves in Figure 3e. In contrast, AgP_2/G and AgP_2 without CNTs deliver poor rate performance and the P electrode shows very poor rate capability and stability, indicating that the interfacial engineering of CNTs significantly improves the stability and rate performance.

The K^+-storage kinetics was analyzed on the basis of the CV measurements to understand the storage characteristics of AgP_2/CNT. Figure 4a shows five CV curves with scan rates ranging from 0.2 to 1.0 mV s^{-1}. Established on the relationship of the peak current (i) and the sweep rate (v: 0.2−1 mV s^{-1}), $i = av^b$. In this equation, a and b are constants in the power law.[44] Generally, a b value of 0.5 indicates a typical diffusion-controlled process, while a b value of 1.0 suggests a surface capacitive-controlled process and the resulting capacity is called a pseudocapacitive-controlled process. With this delineation in mind, parameters a and b are determined from the slope of the $\log(i)-\log(v)$, as presented in Figure 4b. The calculated b value of the AgP_2/CNT is 0.76, indicating that the K^+-storage kinetics occupies a middle ground between capacitive- and diffusion-controlled electrode kinetics.[45] We further employ scan rate-dependent CV curves to explore the capacitive- and diffusion-controlled charge storage contributions, and the total current response (i) at a fixed potential (V) can be based on the following equation: $i = (k_1v) + (k_2v^{1/2})$, where k_1v and $k_2v^{1/2}$ represent the capacitive- and diffusion-controlled processes, respectively.[46] The values of k_1 and k_2 can be calculated by estimating the ratio of capacitive control (k_1v) and diffusion control ($k_2v^{1/2}$) by plotting $i(V)/v^{1/2}$ versus $v^{1/2}$ at a fixed potential. The green area is the proportion of capacitive contribution for the AgP_2/CNT electrode, which is approximately 48.2% at a scan rate of 0.6 mV s^{-1}, as shown in Figure 4c. In addition, Figure 4d shows that the capacitive contributions are 35.0, 41.5, 48.2, 52.1, and 55.6% at scan rates of 0.2, 0.4, 0.6, 0.8, and 1.0 mV s^{-1}, respectively. It is worth mentioning that the capacitive contribution increases gradually with the increase in the scan rate, suggesting that the CNT network structure enhances conductivity and short K^+ diffusion pathways.

In situ XRD and HRTEM were used to ascertain the K^+-storage mechanism of the AgP_2 in Figure 5. The in situ XRD

https://doi.org/10.1021/acsaem.2c03113
ACS Appl. Energy Mater. 2023, 6, 822−831

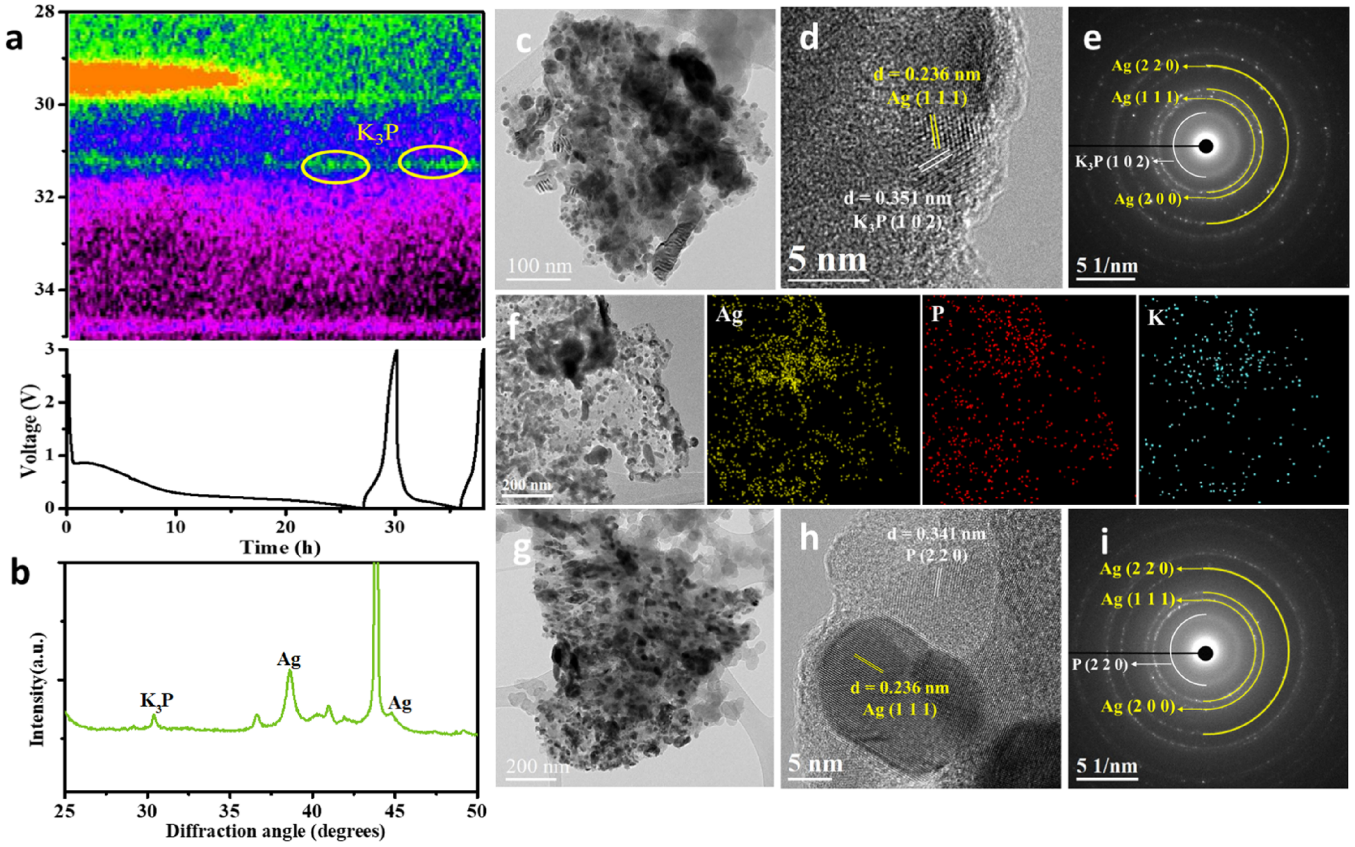

Figure 5. Analysis of the K^+-storage mechanism of the AgP_2. (a) Contour plot of the in situ XRD pattern with a magnified display ranging from 28 to 35° for the initial two cycles. (b) Ex situ XRD of AgP_2 after discharging to 0.01 V. (c) TEM, (d) HRTEM, (e) SAED, and (f) EDS elemental mapping images of the AgP_2 electrode at the initial fully discharged state. (g) TEM, (h) HRTEM, and (i) SAED images of the AgP_2 electrode at the initial fully charged state.

patterns of the two cycles of the cell are depicted in Figure 5a. During the initial cycle, the electrode has been discharged from the open-circuit potential (OCP, ~2.9 V), and the peak of AgP_2 is observed at 29.4°, indicating the (−112) planes of AgP_2. Then, the diffraction peaks of AgP_2 gradually decreased and the intensity become almost insignificant when discharged to a terminal value of 0.01 V. Moreover, consistent with ex situ XRD (Figure 5b), the appearance of new peaks at 31.2° indicates the formation of K_3P (31.2°). During the cell charge, the characteristic peak of K_3P was gradually weakened because of the depotassiation of K_3P. To understand the structural evolution of AgP_2 under different charge/discharge states, we observe the change in the microstructure of bulk AgP_2 (Figure 1c) and the formation of Ag nanocrystals inside the material (Figure 5c,g). Figure 5c−e shows HRTEM and SAED when the electrodes discharged to 0.01 V. The lattice spacings are 0.236 and 0.351 nm, which are assigned to the Ag (111) plane and the K_3P (102) plane, respectively (Figure 5d). The corresponding SAED patterns can also be assigned to the polycrystalline ring of Ag and K_3P. Figure 5g−i shows HRTEM and SAED after charging to 3.0 V. The lattice spacing of Ag is still maintained, and a lattice spacing of 0.341 nm is attributed to the P (220) plane after depotassiation (Figure 5h), which are assigned to the polycrystalline ring of Ag and P through SAED. Furthermore, the EDS mappings (Figure 5f) show that Ag, P, and K elements are homogeneously distributed over the anode material. A similar K^+-storage mechanism in metal phosphides was also reported.[11,47,48] On the basis of the above results, we conjecture the reaction mechanism that AgP_2 decomposes into Ag nanocrystals and K_3P after discharge in the first cycle and the reversible reaction is $K_3P \leftrightarrow P + K$. After cycling, the Ag has no volume change because it does not react with K^+. However, the reversible reaction of $K_3P \leftrightarrow P + K$ has a significant volume change. The difference in volume change between Ag and P leads to the refinement of the overall material to increase the utilization efficiency of P. Moreover, AgP_2 uniformly disperses into the framework of CNTs, effectively combining Ag and P on the surface, providing a large surface area to facilitate the penetration of electrolytes, and improving the conductivity. Figure S5a shows the SEM image of AgP_2/CNT after 50 cycles. The size of the active material has decreased significantly and uniformly encapsulated in CNTs, validating that CNTs effectively trap the material.

The in situ EIS was analyzed at various potentials at the AgP_2/CNT electrode charge/discharge processes in Figure 6, confirming the electrochemical kinetics of AgP_2/CNT. Figure 6a,b presents the Nyquist plots recorded during the in situ EIS analysis of the AgP_2/CNT electrode in the initial cycle, including OCV, 1.5, 1.3, 1.1, 0.9, 0.6, 0.3, and 0.01 V at the discharged process and 0.5, 0.7, 0.9, 1.1, 1.6, 2.0, 2.5, and 3.0 V at the charged process. As the electrode discharged from OCV to 0.9 V, the resistance decreased significantly, which is attributed to in situ formed Ag nanocrystals. When discharging to 0.6 V, the resistance increases slightly and no obvious resistance changes until the discharge to 0.01 V. The results imply that P gradually reacts with K^+ to generate K_3P, which slightly increases the resistance of the material. At the end of the charging, the resistance has a significant downward trend,

https://doi.org/10.1021/acsaem.2c03113
ACS Appl. Energy Mater. 2023, 6, 822−831

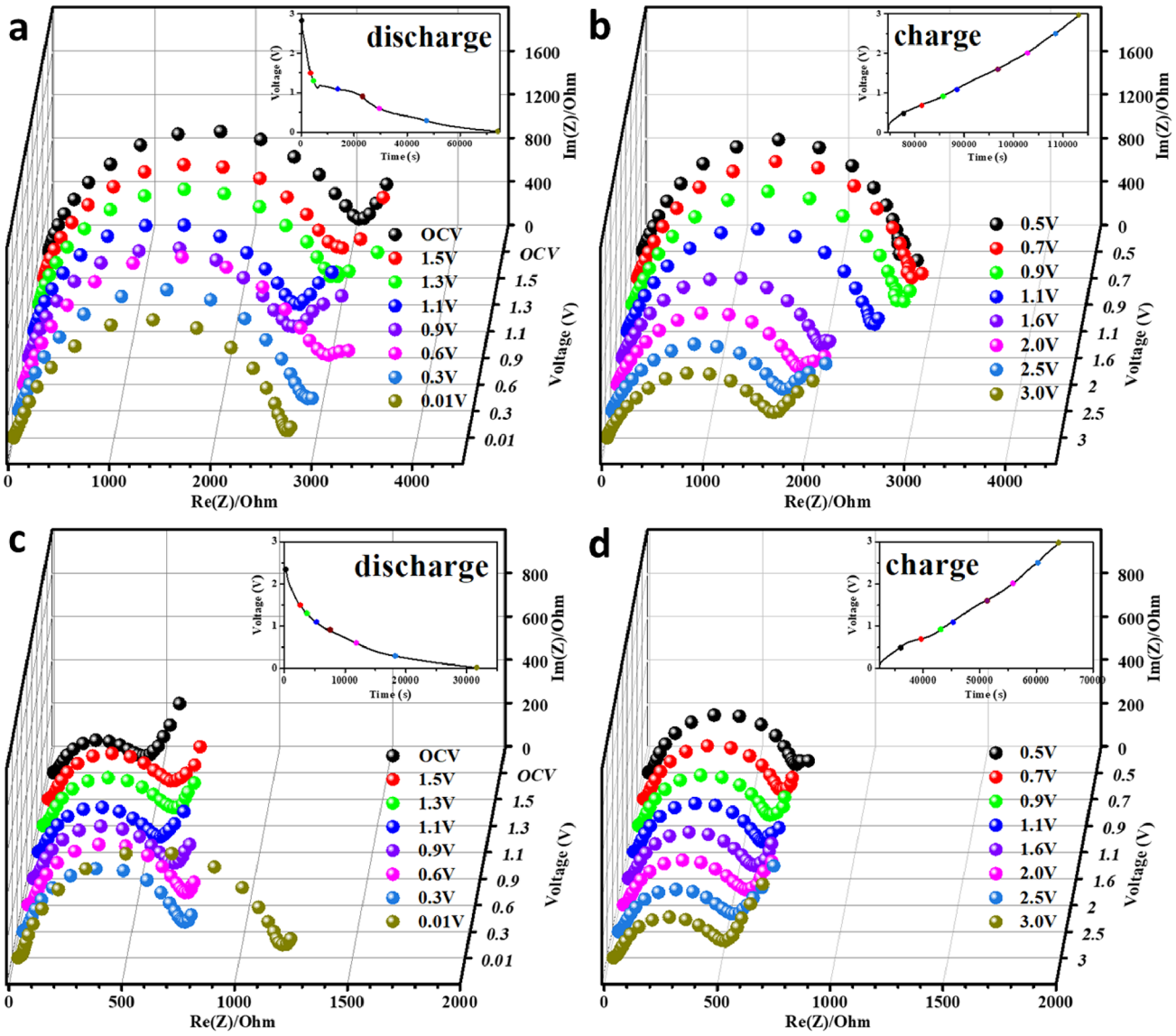

Figure 6. In situ EIS of the AgP_2/CNT electrode for the (a, b) 1st cycle and (c, d) 20th cycle at pre-selected potentials, inset: charge/discharge curves.

indicating that K_3P gradually decomposes to P and the formation of ion channels effectively improves the material conductivity. Figure 6c,d presents the Nyquist plots recorded during the in situ EIS analysis of the AgP_2/CNT electrode in the 20th cycle. As K_3P forms during discharge to 0.3 V, the resistance gradually increases. Upon further discharging to 0.01 V, K_3P blocks the contact between the electrolyte and CNTs, which sharply increases the resistance. As the electrode charges to 3.0 V, the decomposition of K_3P reduces the resistance. Figure S7 shows the EIS of AgP_2/CNT before and after the 20th cycle. The refinement of the material becomes more complete during volume contraction with cycles, which reduced the particle size and uniformly distributed on the CNTs (Figure S5a), leading to the R_{ct} decreased during cycles.

The interface engineering of CNTs and Ag nanocrystals has the following advantages: (i) enhanced electronic conductivity of the material, (ii) enhanced structural stability, and (iii) adsorption/desorption capability of high K^+ into a large surface area with active sites. We expect these advantages to promote fast K^+ transport kinetics, which is beneficial for the performance of the PIHC. To confirm the effects, the PIHC composed of a commercial-activated carbon (AC) cathode and a AgP_2/CNT anode was assembled (designated as AgP_2/CNT//AC), as shown in Figure 7. Upon charging, the FSI^- anions in the electrolyte adsorb on the AC cathode while the adsorption of K^+ absorbs on the AgP_2/CNT anode side. Figure 7a shows the working window of AgP_2/CNT//AC (bottom) as well as the individual electrodes (top). The theoretical charge/discharge curves of the AC half-cell are 2.00−4.00 V and the AgP_2/CNT half-cell at 0.01−3.00 V. Therefore, the working window of AgP_2/CNT//AC is from 0.01 to 4.00 V. However, the FIS-based electrolyte decomposits in the operating voltage of 4.0 V.[49] To achieve high energy/power densities and stability, the operating window of the PIHC is set from 0.1 to 3.5 V. Figure 7b shows the rate performance of the PIHC full cell, and based on the total mass of AC and AgP_2/CNT, the AgP_2/CNT//AC full cells display energy densities of 85.9, 76.2, 69.2, 61.5, 53.2, and 37.3 Wh kg^{-1} at current densities of 0.2, 0.5, 1, 2, 3, and 5 A g^{-1}, respectively. The charge/discharge curves of the PIHC at different current

https://doi.org/10.1021/acsaem.2c03113
ACS Appl. Energy Mater. 2023, 6, 822−831

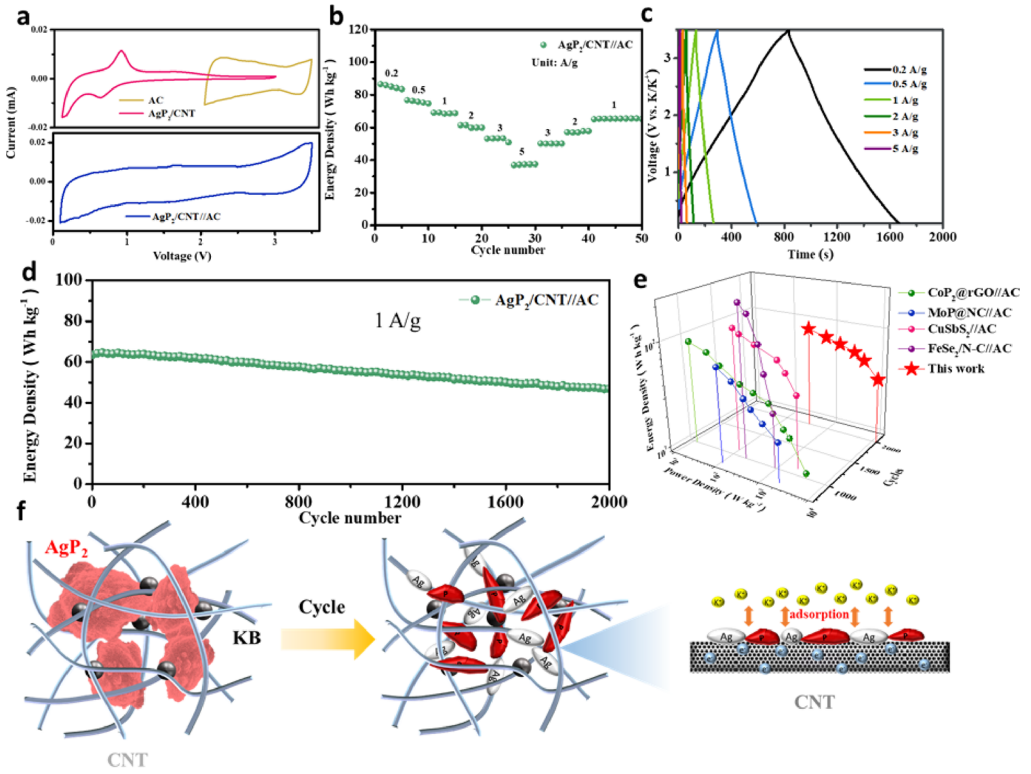

Figure 7. Electrochemical characteristics of AgP_2/CNT//AC PHIC. (a) CV profiles of AC, AgP_2/CNT half-cell (top), and AgP_2/CNT//AC PIHC (bottom). (b) Rate performance of AgP_2/CNT//AC full cells cycled at various current densities from 200 to 5000 mA g^{-1}. (c) Charge/discharge curve of AgP_2/CNT//AC at various current densities from 200 to 5000 mA g^{-1}. (d) Cycling performance of AgP_2/CNT//AC full cells at a current density of 1000 mA g^{-1}. (e) Comparison of the 3D Ragone plot of AgP_2/CNT//AC full cells. (f) Illustrative image of the in situ formed Ag nanocrystals from AgP_2/CNT and promoting adsorption/desorption of K^+ in the PIHC.

densities are shown in Figure 7c, which exhibit an almost triangular shape with relatively linear voltage-time plots, revealing a good capacitive behavior. Moreover, as shown in Figure 7d, the long-term cycle performance of the AgP_2/CNT//AC PIHC achieves 2000 cycles with an energy density of 46.3 Wh kg^{-1} at a high current density of 1 A g^{-1}. It is revealed that AgP_2/CNT//AC is an energy storage device suitable for hybrid capacitor applications. The 3D plots based on the energy density, power density, and cycle number of AgP_2/CNT//AC and other materials in PIHCs, including CoP_2@rGO//AC,[18] MoP@NC//AC,[50] $CuSbS_2$//AC,[51] and $FeSe_2$/N-C//AC,[52] are presented in Figure 7e. The AgP_2/CNT//AC PIHC exhibits the best performance in terms of power density, cycle life, and energy density with the recently reported PIHCs. Figure 7f shows the illustrative mechanism of in situ formed Ag nanocrystals from AgP_2/CNT. After electrochemical activation, the bulk AgP_2 decomposes to Ag nanocrystals and P compositing with CNTs. The composites of CNTs, Ag nanocrystals, and P effectively increase the contact area with the electrolyte as well as shorten the K^+ diffusion distance and increase electronic conduction between the active material and current collector. In addition, benefiting from the barrier of Ag nanocrystals and CNTs avoids the cluster of P that maintains a high specific surface with active sites, which promote the transmission of electrons and adsorption/desorption of K^+. In view of the above discussion, the interfacial engineering of Ag and CNTs exhibits an extraordinarily energy/power density of 37.3 Wh kg^{-1}/12207.3 W kg^{-1}, respectively, in phosphide-based PIHCs.

4. CONCLUSIONS

In conclusion, we demonstrate that interfacial engineering of CNTs and Ag nanocrystals improves the energy/power density and cycling stability of metal phosphide PIHCs. We performed ex situ TEM and in situ XRD studies to confirm the unique AgP_2 reaction mechanism, in which in situ formed Ag nanocrystals were observed to play a key role in effectively reducing resistance and increasing active sites in phosphide substrates. Furthermore, the high structural stability framework of CNTs not only improves electronic conduction but also provides a surface area for bonding with Ag nanocrystals and P, thereby enhancing the contact interface with the electrolyte. The above results reveal important advantages of interfacial engineering of Ag nanocrystals and CNTs, including (i) enhanced electronic conductivity of the material, (ii) enhanced structural stability of the CNT framework, and (iii) providing a large surface area and active sites for the adsorption/desorption of K^+. The PIHC with the AgP_2/CNT//AC anode exhibited an extremely high energy/power density of 37.3 Wh kg^{-1}/12207.3 W kg^{-1}, respectively, and excellent cycling performance (46.3 Wh kg^{-1} after 2000 cycles). Importantly, the strategy to design in situ formed Ag nanocrystals and CNT frameworks for metal phosphides is relevant to other materials with low electronic conductivity and poor structural stability and thus is expected to be of great value in expanding new prospects for various applications.

https://doi.org/10.1021/acsaem.2c03113
ACS Appl. Energy Mater. 2023, 6, 822−831

■ ASSOCIATED CONTENT

Supporting Information

The Supporting Information is available free of charge at https://pubs.acs.org/doi/10.1021/acsaem.2c03113.

SEM of CNT and Ketjen Black, XPS fully scanned spectra of AgP_2/CNT, cycle performance of AgP_2/CNT at a current density of 100 mA g^{-1}, EDS mapping images of Ag and P in the AgP_2 electrode after charging to 3.0 V, the SEM image of the AgP_2/CNT electrode after 20 cycles, and EIS plots of AgP_2/CNT before and after 20 cycles (PDF)

■ AUTHOR INFORMATION

Corresponding Author

Hsing-Yu Tuan − *Department of Chemical Engineering, National Tsing Hua University, Hsinchu 30013, Taiwan;* orcid.org/0000-0003-2819-2270; Phone: (886)3-571-5131; Email: hytuan@che.nthu.edu.tw

Authors

Jia-Zheng Yen − *Department of Chemical Engineering, National Tsing Hua University, Hsinchu 30013, Taiwan*

Che-Bin Chang − *Department of Chemical Engineering, National Tsing Hua University, Hsinchu 30013, Taiwan*

Kai-Siang Jhang − *Department of Chemical Engineering, National Tsing Hua University, Hsinchu 30013, Taiwan*

Complete contact information is available at: https://pubs.acs.org/10.1021/acsaem.2c03113

Notes

The authors declare no competing financial interest.

■ ACKNOWLEDGMENTS

This work was financially supported by the 2030 Cross-Generation Young Scholars Program by the Ministry of Science and Technology, Taiwan (MOST 111-2628-E-007-008). H.-Y.T. also acknowledges the financial support of National Tsing Hua University, Taiwan, through the grant 111QI030E1.

■ REFERENCES

(1) Armand, M.; Tarascon, J.-M. Building better batteries. *Nature* **2008**, *451*, 652−657.

(2) Wu, Y.; Zhang, C.; Zhao, H.; Lei, Y. Recent advances in ferromagnetic metal sulfides and selenides as anodes for sodium-and potassium-ion batteries. *J. Mater. Chem. A* **2021**, *9*, 9506−9534.

(3) Eftekhari, A.; Jian, Z.; Ji, X. Potassium secondary batteries. *ACS Appl. Mater. Interfaces* **2017**, *9*, 4404−4419.

(4) Rajagopalan, R.; Tang, Y.; Ji, X.; Jia, C.; Wang, H. Advancements and challenges in potassium ion batteries: a comprehensive review. *Adv. Funct. Mater.* **2020**, *30*, 1909486.

(5) Ji, B.; Zhang, F.; Song, X.; Tang, Y. A novel potassium-ion-based dual-ion battery. *Adv. Mater.* **2017**, *29*, 1700519.

(6) Pramudita, J. C.; Sehrawat, D.; Goonetilleke, D.; Sharma, N. An initial review of the status of electrode materials for potassium-ion batteries. *Adv. Energy Mater.* **2017**, *7*, 1602911.

(7) Feng, Y.; Xu, M.; He, T.; Chen, B.; Gu, F.; Zu, L.; Meng, R.; Yang, J. CoPSe: A New Ternary Anode Material for Stable and High-Rate Sodium/Potassium-Ion Batteries. *Adv. Mater.* **2021**, *33*, 2007262.

(8) Chang, W. C.; Wu, J. H.; Chen, K. T.; Tuan, H. Y. Red phosphorus potassium-ion battery anodes. *Adv. Sci.* **2019**, *6*, 1801354.

(9) Liu, D.; Huang, X.; Qu, D.; Zheng, D.; Wang, G.; Harris, J.; Si, J.; Ding, T.; Chen, J.; Qu, D. Confined phosphorus in carbon nanotube-backboned mesoporous carbon as superior anode material for sodium/potassium-ion batteries. *Nano Energy* **2018**, *52*, 1−10.

(10) Yang, D.; Liu, C.; Rui, X.; Yan, Q. Embracing high performance potassium-ion batteries with phosphorus-based electrodes: a review. *Nanoscale* **2019**, *11*, 15402−15417.

(11) Bai, J.; Xi, B.; Mao, H.; Lin, Y.; Ma, X.; Feng, J.; Xiong, S. One-step construction of N, P-codoped porous carbon sheets/CoP hybrids with enhanced lithium and potassium storage. *Adv. Mater.* **2018**, *30*, 1802310.

(12) Huang, S.-B.; Hsieh, Y.-Y.; Chen, K.-T.; Tuan, H.-Y. Flexible nanostructured potassium-ion batteries. *Chem. Eng. J.* **2021**, *416*, No. 127697.

(13) Zhao, X.; Wang, W.; Hou, Z.; Wei, G.; Yu, Y.; Zhang, J.; Quan, Z. SnP0. 94 nanoplates/graphene oxide composite for novel potassium-ion battery anode. *Chem. Eng. J.* **2019**, *370*, 677−683.

(14) Lu, S.-C.; Hsiao, M.-C.; Yorulmaz, M.; Wang, L.-Y.; Yang, P.-Y.; Link, S.; Chang, W.-S.; Tuan, H.-Y. Single-crystalline copper nano-octahedra. *Chem. Mater.* **2015**, *27*, 8185−8188.

(15) Tang, J.; Wang, C.-Y.; Xiu, F.; Hong, A. J.; Chen, S.; Wang, M.; Zeng, C.; Yang, H.-J.; Tuan, H.-Y.; Tsai, C.-J.; Chen, L. J.; Wang, K. L. Single-crystalline Ni_2Ge/Ge/Ni_2Ge nanowire heterostructure transistors. *Nanotechnology* **2010**, *21*, No. 505704.

(16) Yang, H.-J.; Chen, C.-Y.; Yuan, F.-W.; Tuan, H.-Y. Designed synthesis of solid and hollow Cu2−x Te nanocrystals with tunable near-infrared localized surface plasmon resonance. *J. Phys. Chem. C* **2013**, *117*, 21955−21964.

(17) Zhou, D.; Yi, J.; Zhao, X.; Yang, J.; Lu, H.; Fan, L.-Z. Confining ultrasmall CoP nanoparticles into nitrogen-doped porous carbon via synchronous pyrolysis and phosphorization for enhanced potassium-ion storage. *Chem. Eng. J.* **2021**, *413*, No. 127508.

(18) Wang, Y.; Zhang, Z.; Wang, G.; Yang, X.; Sui, Y.; Du, F.; Zou, B. Ultrafine Co_2P nanorods wrapped by graphene enable a long cycle life performance for a hybrid potassium-ion capacitor. *Nanoscale Horiz.* **2019**, *4*, 1394−1401.

(19) Chang, G.; Zhao, Y.; Dong, L.; Wilkinson, D. P.; Zhang, L.; Shao, Q.; Yan, W.; Sun, X. A.; Zhang, J. A review of phosphorus and phosphides as anode materials for advanced sodium-ion batteries. *J. Mater. Chem. A* **2020**, *8*, 4996−5048.

(20) Wu, Y.; Huang, H. B.; Feng, Y.; Wu, Z. S.; Yu, Y. The promise and challenge of phosphorus-based composites as anode materials for potassium-ion batteries. *Adv. Mater.* **2019**, *31*, 1901414.

(21) Chen, C.; Wen, Y.; Hu, X.; Ji, X.; Yan, M.; Mai, L.; Hu, P.; Shan, B.; Huang, Y. Na+ intercalation pseudocapacitance in graphene-coupled titanium oxide enabling ultra-fast sodium storage and long-term cycling. *Nat. Commun.* **2015**, *6*, 1−8.

(22) Yang, B.; Chen, J.; Liu, L.; Ma, P.; Liu, B.; Lang, J.; Tang, Y.; Yan, X. 3D nitrogen-doped framework carbon for high-performance potassium ion hybrid capacitor. *Energy Storage Mater.* **2019**, *23*, 522−529.

(23) Chang, C.-H.; Chen, K.-T.; Hsieh, Y.-Y.; Chang, C.-B.; Tuan, H.-Y. Crystal facet and architecture engineering of metal oxide nanonetwork anodes for high-performance potassium ion batteries and hybrid capacitors. *ACS Nano* **2022**, *16*, 1486−1501.

(24) Lin, W.-C.; Yang, Y.-C.; Tuan, H.-Y. Ternary chalcogenide anodes for high-performance potassium-ion batteries and hybrid capacitors via composition-mediated bond softening and intermediate phase. *Energy Storage Mater.* **2022**, *51*, 38−53.

(25) Hsieh, Y.-Y.; Tuan, H.-Y. Architectural van der Waals Bi_2S_3/Bi_2Se_3 topological heterostructure as a superior potassium-ion storage material. *Energy Storage Mater.* **2022**, *51*, 789−805.

(26) Yue, L.; Liang, J.; Wu, Z.; Zhong, B.; Luo, Y.; Liu, Q.; Li, T.; Kong, Q.; Liu, Y.; Asiri, A. M.; Guo, X.; Sun, X. Progress and perspective of metal phosphide/carbon heterostructure anodes for rechargeable ion batteries. *J. Mater. Chem. A* **2021**, *9*, 11879−11907.

(27) Wang, Y.; Wang, Z.; Chen, Y.; Zhang, H.; Yousaf, M.; Wu, H.; Zou, M.; Cao, A.; Han, R. P. Hyperporous sponge interconnected by hierarchical carbon nanotubes as a high-performance potassium-ion battery anode. *Adv. Mater.* **2018**, *30*, 1802074.

(28) Chong, S.; Sun, L.; Shu, C.; Guo, S.; Liu, Y.; Wang, W. A.; Liu, H. K. Chemical bonding boosts nano-rose-like MoS_2 anchored on reduced graphene oxide for superior potassium-ion storage. *Nano Energy* **2019**, *63*, No. 103868.
(29) Yu, X.; Lu, B.; Xu, Z. Super long-life supercapacitors based on the construction of nanohoneycomb-like strongly coupled $CoMoO_4$−3D graphene hybrid electrodes. *Adv. Mater.* **2014**, *26*, 1044−1051.
(30) Li, S.; Cao, J.; Wang, T.; Wang, L.; Deng, H.; Zhang, Q.; Cheng, Y.; Zhu, J.; Lu, B. Intercalation and covalent bonding strategies for constructing a stable cathode for high-energy density and long-cycling potassium-organic batteries. *Chem. Eng. J.* **2022**, *431*, No. 133215.
(31) Zhang, W.; Liu, Y.; Guo, Z. Approaching high-performance potassium-ion batteries via advanced design strategies and engineering. *Sci. Adv.* **2019**, *5*, No. eaav7412.
(32) Zardkhoshoui, A. M.; Davarani, S. S. H.; Ashtiani, M. M.; Sarparast, M. Designing an asymmetric device based on graphene wrapped yolk−double shell $NiGa_2S_4$ hollow microspheres and graphene wrapped FeS_2−$FeSe_2$ core−shell cratered spheres with outstanding energy density. *J. Mater. Chem. A* **2019**, *7*, 10282−10292.
(33) Li, S. Y.; Deng, H. L.; Chu, Z. L.; Wang, T.; Wang, L.; Zhang, Q. S.; Cao, J. H.; Cheng, Y. L.; Huang, Y. Q.; Zhu, J. Fast-Charging Nonaqueous Potassium-Ion Batteries Enabled by Rational Construction of Oxygen-Rich Porous Nanofiber Anodes. *ACS Appl. Mater. Interfaces* **2021**, *13*, 50005−50016.
(34) Khan, N.; Han, G.; Mazari, S. A. Carbon nanotubes-based anode materials for Potassium ion batteries: A review. *J. Electroanal. Chem.* **2022**, No. 116051.
(35) Chen, K.-T.; Yang, Y.-C.; Lyu, L.-M.; Lu, M.-Y.; Tuan, H.-Y. In situ formed robust submicron-sized nanocrystalline aggregates enable highly-reversible potassium ion storage. *Nano Energy* **2021**, *88*, No. 106233.
(36) Ye, F.; Lu, D.; Gui, X.; Wang, T.; Zhuang, X.; Luo, W.; Huang, Y. Atomic layer deposition of core-shell structured V_2O_5@ CNT sponge as cathode for potassium ion batteries. *J. Materiomics* **2019**, *5*, 344−349.
(37) Wang, Z.; Gao, W.; Ding, C.; Qi, H.; Kang, S.; Cui, L. Boosting potassium-ion storage in large-diameter carbon nanotubes/MoP hybrid. *J. Colloid Interface Sci.* **2021**, *584*, 875−884.
(38) Luo, Y.; Wang, C.; Wang, X. Fast energy storage performance of $CoFe_2O_4$/CNTs hybrid aerogels for potassium ion battery. *J. Colloid Interface Sci.* **2021**, *600*, 820−827.
(39) Chang, C.-B.; Tsai, C.-Y.; Chen, K.-T.; Tuan, H.-Y. Solution-grown phosphorus-hyperdoped silicon nanowires/carbon nanotube bilayer fabric as a high-performance lithium-ion battery anode. *ACS Appl. Energy Mater.* **2021**, *4*, 3160−3168.
(40) Gao, J.; Wang, G.; Wang, W.; Yu, L.; Peng, B.; El-Harairy, A.; Li, J.; Zhang, G. Engineering Electronic Transfer Dynamics and Ion Adsorption Capability in Dual-Doped Carbon for High-Energy Potassium Ion Hybrid Capacitors. *ACS Nano* **2022**, *16*, 6255−6265.
(41) Zhu, Y. E.; Yang, L.; Sheng, J.; Chen, Y.; Gu, H.; Wei, J.; Zhou, Z. Fast sodium storage in TiO_2@ CNT@ C nanorods for high-performance Na-ion capacitors. *Adv. Energy Mater.* **2017**, *7*, 1701222.
(42) Jiang, Y.; Shen, Y.; Dong, J.; Tan, S.; Wei, Q.; Xiong, F.; Li, Q.; Liao, X.; Liu, Z.; An, Q.; Mai, L. Surface pseudocapacitive mechanism of molybdenum phosphide for high-energy and high-power sodium-ion capacitors. *Adv. Energy Mater.* **2019**, *9*, 1900967.
(43) Zhang, M.; Hu, R.; Liu, J.; Ouyang, L.; Yang, L.; Fang, F.; Zhu, M. AgP_2/C as an anode for high rate performance lithium-ion batteries. *J. Alloys Compd.* **2018**, *762*, 246−253.
(44) Kim, H.-S.; Cook, J. B.; Lin, H.; Ko, J. S.; Tolbert, S. H.; Ozolins, V.; Dunn, B. Oxygen vacancies enhance pseudocapacitive charge storage properties of MoO_3− x. *Nat. Mater.* **2017**, *16*, 454−460.
(45) Bard, A.J.; Faulkner, L.R.; White, H.S., *Electrochemical methods: fundamentals and applications*; John Wiley & Sons, 2022.
(46) Chao, D.; Zhu, C.; Yang, P.; Xia, X.; Liu, J.; Wang, J.; Fan, X.; Savilov, S. V.; Lin, J.; Fan, H. J. Array of nanosheets render ultrafast and high-capacity Na-ion storage by tunable pseudocapacitance. *Nat. Commun.* **2016**, *7*, 1−8.
(47) Ji, S.; Song, C.; Li, J.; Hui, K. S.; Deng, W.; Wang, S.; Li, H.; Dinh, D. A.; Fan, X.; Wu, S.; Zhang, J.; Chen, F.; Shao, Z.; Hui, K. N. Metal Phosphides Embedded with In Situ-Formed Metal Phosphate Impurities as Buffer Materials for High-Performance Potassium-Ion Batteries. *Adv. Energy Mater.* **2021**, *11*, 2101413.
(48) Li, L.; Hu, Z.; Lu, Y.; Zhao, S.; Zhang, Q.; Liu, Q.; Yan, Z.; Chou, S.-L. CuP_2 as high-capacity and long-cycle-life anode for potassium-ion batteries. *J. Energy Chem.* **2021**, *63*, 246−252.
(49) Xiao, N.; McCulloch, W. D.; Wu, Y. Reversible dendrite-free potassium plating and stripping electrochemistry for potassium secondary batteries. *J. Am. Chem. Soc.* **2017**, *139*, 9475−9478.
(50) Zong, W.; Chui, N.; Tian, Z.; Li, Y.; Yang, C.; Rao, D.; Wang, W.; Huang, J.; Wang, J.; Lai, F. Ultrafine MoP nanoparticle splotched nitrogen-doped carbon nanosheets enabling high-performance 3D-printed potassium-ion hybrid capacitors. *Adv. Sci.* **2021**, *8*, 2004142.
(51) Chang, C.-B.; Chen, K.-T.; Tuan, H.-Y. Large-scale synthesis of few-layered copper antimony sulfide nanosheets as electrode materials for high-rate potassium-ion storage. *J. Colloid Interface Sci.* **2022**, *608*, 984−994.
(52) Ge, J.; Wang, B.; Wang, J.; Zhang, Q.; Lu, B. Nature of $FeSe_2$/N-C anode for high performance potassium ion hybrid capacitor. *Adv. Energy Mater.* **2020**, *10*, 1903277.

https://doi.org/10.1021/acsaem.2c03113
ACS Appl. Energy Mater. 2023, 6, 822−831